

Modification of fluid inclusions in quartz by deviatoric stress. III: Influence of principal stresses on inclusion density and orientation

A. Tarantola · L. W. Diamond · H. Stünitz ·
A. Thust · M. Pec

Received: 17 August 2011 / Accepted: 8 April 2012 / Published online: 27 April 2012
© Springer-Verlag 2012

Abstract Extraction of useful geochemical, petrologic and structural information from deformed fluid inclusions is still a challenge in rocks displaying moderate plastic strain. In order to better understand the inclusion modifications induced by deviatoric stresses, six deformation experiments were performed with a Griggs piston-cylinder apparatus. Natural NaCl–H₂O inclusions in an oriented quartz crystal were subjected to differential stresses of 250–470 MPa at 700–900 °C and at 700–1,000 MPa confining pressure. Independently of the strain rate and of the crystallographic orientation of the quartz, the inclusions became dismembered and flattened within a crystallographic cleavage plane subperpendicular to σ_1 . The neonate (newly formed) inclusions that result from dismemberment have densities that tend towards equilibrium with $P_{\text{fluid}} = \sigma_1$ at T_{shearing} . These results permit

ambiguities in earlier deformation experiments on CO₂–H₂O–NaCl to be resolved. The results of the two studies converge, indicating that density changes in neonate inclusions are promoted by high differential stresses, long periods at high P and high T , and fluid compositions that maximize quartz solubility. Neonates spawned from large precursor inclusions show greater changes in density than those spawned from small precursors. These findings support the proposal that deformed fluid inclusions can serve as monitors of both the orientation and magnitude of deviatoric stresses during low-strain, ductile deformation of quartz-bearing rocks.

Keywords Fluid inclusions · Re-equilibration · Isochores · Crystal plasticity · Deformation · Deviatoric stress

Communicated by J. L. R. Touret.

Electronic supplementary material The online version of this article (doi:10.1007/s00410-012-0749-1) contains supplementary material, which is available to authorized users.

A. Tarantola (✉)
G2R-CNRS, Lorraine University, BP 70239,
54506 Vandœuvre-lès-Nancy, France
e-mail: alexandre.tarantola@g2r.uhp-nancy.fr

L. W. Diamond
Fluid-Rock Interaction Group, Institute Geological Sciences,
University of Bern, Baltzerstrasse 3, 3012 Bern, Switzerland

H. Stünitz
Department of Geology, University of Tromsø,
Dramsveien 201, 9037 Tromsø, Norway

A. Thust · M. Pec
Department of Geosciences, Basel University,
Bernoullistr. 32, 4056 Basel, Switzerland

Introduction

Fluid inclusions in undeformed quartz crystals generally preserve the properties of the parent fluid from the time of its entrapment, because their crystalline surroundings are rigid and normally impermeable to chemical exchange (exceptions being the diffusion of H₂, He and possibly H₂O under extreme conditions; Morgan et al. 1993; Mavrogenes and Bodnar 1994; Hall and Sterner 1995; Bakker and Jansen 1991, 1994; Sterner et al. 1995; Diamond et al. 2010). Accordingly, fluid inclusions in undeformed quartz have yielded a wealth of information on palaeofluids in the crust.

In contrast, quartz grains that have experienced high plastic deformation, such as those that compose schists, gneisses and mylonites, are typically devoid of any microscopic inclusions that predate the deformation (e.g.

Kerrich 1976; Wilkins and Barkas 1978), although sub-microscopic inclusions, observable in TEM, may be present (Bakker and Jansen 1994). Extensive crystal-plastic deformation is known to obliterate fluid inclusions during dynamic recrystallization when grain boundaries migrate (e.g. Hollister 1990; Johnson and Hollister 1995; Schmatz et al. 2011).

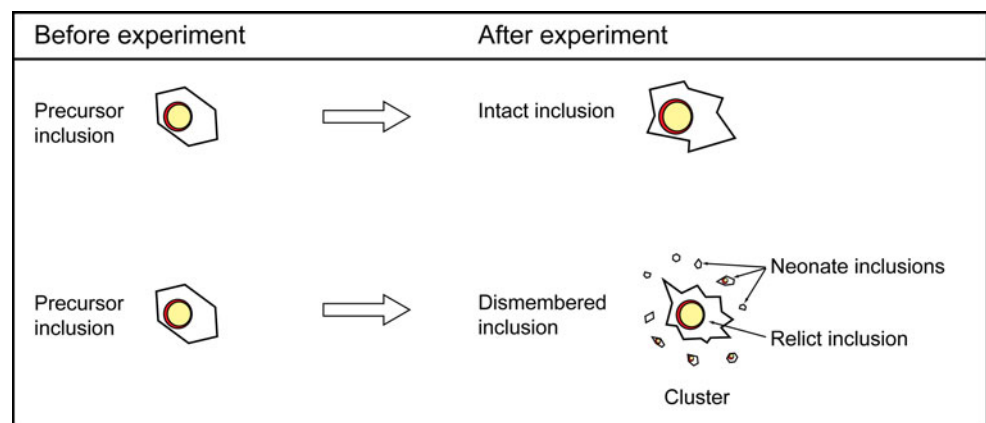
Moderately strained rocks, such as plastically deformed hydrothermal quartz veins in shear zones, very commonly contain fluid inclusions that are obviously deformed yet still preserved. Such inclusions lie between the above extremes of pristine preservation and complete annihilation. In these cases, it would be useful to know whether the deformed inclusions retain information on the chemical composition and density of the pre-deformation palaeofluids and whether they record conditions of the plastic deformation itself. The recent experimental studies of Tarantola et al. (2010) and Diamond et al. (2010) have been conducted to provide the necessary theoretical basis on which such questions may be answered. The experiments have managed to reproduce the shapes and associated microstructures of naturally deformed fluid inclusions by subjecting single quartz crystals containing CO₂–H₂O–NaCl inclusions to high deviatoric stresses. The deformation experiments were carried out at 700 °C and ~600 MPa confining pressure in a Griggs piston-cylinder apparatus. It was found that inclusions that survive the resulting semi-plastic strain intact do indeed preserve their pre-deformation fluid properties, even though they adopt irregular shapes (Fig. 1). However, most of the inclusions in the experiments became dismembered into disc-shaped clusters of tiny, newly formed (“neonate”) inclusions, surrounding irregularly shaped relicts of the precursor inclusions (Fig. 1). The thousands of discoid inclusions in each deformed sample define a planar fabric, which lies subperpendicular to σ_1 . Tarantola et al. (2010) suggested that the direction of σ_1 can therefore be deduced from the corresponding fabric in natural samples. Whereas the relict

inclusions preserve the original chemical composition, their densities bear no obvious relation to the P – T history of the sample. The neonates, in contrast, had lost H₂O and their densities had increased markedly, approaching the value consistent with the experimentally imposed principal stress, σ_1 . Although there were some methodological ambiguities regarding the interpretation of the stress values and fluid inclusion isochores, Diamond et al. (2010) suggested that this finding may be applicable to natural samples. If the temperature of deformation is known, its intersection with the isochores of neonate inclusions defines the absolute magnitude of the principal stress, σ_1 .

The latter result is of considerable interest to studies of rock deformation. However, prior to being applied to nature, the ambiguities in the stress values and isochores in the experiments of Diamond et al. (2010) need to be resolved. In the present study, we first re-examine the issue of stress in the Griggs apparatus. Second, we report the results of 6 new experiments carried out using a similar approach to Tarantola et al. (2010) and Diamond et al. (2010), but on a different natural quartz crystal containing H₂O–NaCl inclusions. The compositional simplicity of these inclusions affords an unambiguous construction of their isochores. This allows verification of the idea that the internal pressure of neonate fluid inclusions corresponds to the imposed σ_1 . Third, based on this verification, the isochores constructed in the experiments of Diamond et al. (2010) are corrected. Finally, we apply the correct stresses and isochores to the results of Diamond et al. (2010), thereby settling the open questions in that study.

This treatment shows that the inclusions in the new experiments are consistent with the earlier studies, but that in part they represent more advanced steps along a progression in modifications of density, composition and shape. Collectively, these results lend strong support to the idea that deformed fluid inclusions can serve as monitors of both the direction and magnitude of σ_1 during low-strain, crystal-plastic deformation of rocks.

Fig. 1 Nomenclature of fluid inclusions deformed by deviatoric stress, after Tarantola et al. (2010)



Stress conditions during Griggs piston-cylinder experiments

Part of ambiguity noted by Diamond et al. (2010) in their experiments arises from the uncertainty in the maximum stress values experienced by the samples in the Griggs piston-cylinder apparatus. The apparatus allows samples to be heated to high temperature and subjected to two types of stress regimes. First, high hydrostatic stresses can be imposed, resulting in the present case in purely elastic deformation of the inclusion-bearing quartz samples. Second, in addition to the hydrostatic confining pressure, uniaxial compressive stress can be applied along the vertical axis of the sample to induce permanent, crystal-plastic deformation. The difference between the axial compressive stress (σ_1) and the radially symmetric hydrostatic confining pressure (σ_3) defines the deviatoric differential stress ($\Delta\sigma = \sigma_1 - \sigma_3$; this external, directed stress is not to be confused with the differential pressure between the inside of the fluid inclusions and the outside of the crystal). The axial stress is transmitted by a WC piston that is driven through a top lead disc onto a series of alumina pistons, which in turn transmit the stress to the underlying sample (Fig. 2a). Either a constant load can be applied to the piston via a servo-driven-motor, which results in variable strain rates of the sample, or the piston can be driven at a constant speed to maintain a constant displacement rate, which results in a constant rate of sample shortening (strain). The latter is the common approach in most deformation studies. However, all the experiments reported by Tarantola et al. (2010) and Diamond et al. (2010), and 3 of the 6 experiments in the present study, were carried out under constant

load so as to fix σ_1 for the duration of the runs. The three remaining experiments reported here were performed under constant displacement rates ($\sim 10^{-5} \text{ mm s}^{-1}$). They were not explicitly designed for this study, and their methodology is not optimal. However, their results turn out to be instructive and surprisingly consistent with all our previous experiments.

In the constant-load experiments of Tarantola et al. (2010) and Diamond et al. (2010), the forces on the sample were assumed to be the same as in constant displacement-rate experiments. However, the clear, systematic results of the new experiments prompted us to question this assumption and to revise it according to the following reasoning. In constant displacement-rate experiments (Fig. 2b), the σ_1 -piston is driven continuously through the lead disc. Thus, throughout the experiment, the force applied to the σ_1 -piston is partitioned into the work of deforming the sample, into the drag forces acting on the pistons, and into the work of deforming the lead via viscous deformation (Fig. 2b, thick black arrows). The axial stress on the sample is therefore lower than the nominal stress applied to the σ_1 -piston itself, and its value must be corrected from the so-called bend- and hit-points in the stress-time records of the experiments (Renner 1996; Holyoke and Kronenberg 2010).

Conversely, in our constant-load experiments (Fig. 2c), viscous deformation and drag forces of the lead disc are relaxed before the peak stress is reached because of the very slow rate of the piston advancement. The piston remains in a virtually static position for the duration of the experiments, so that the relaxation of drag forces and deformation of the lead is compensated by additional

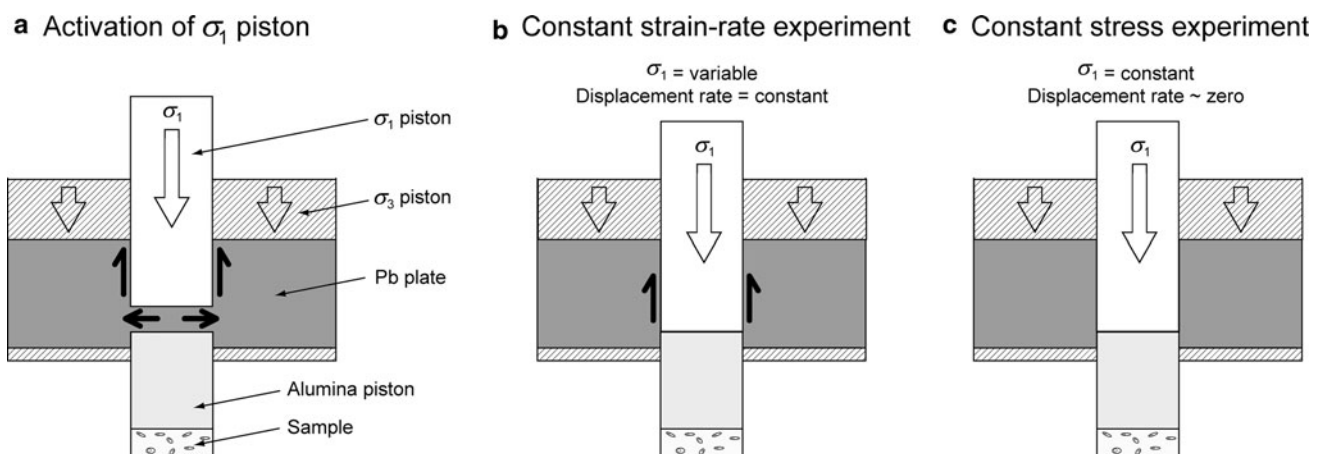


Fig. 2 Schematic cross-sections through the Griggs apparatus illustrating frictional drag of the lead (Pb) plate (thick black arrows) during the deformation experiments. **a** During initiation of an experiment, the σ_1 piston is driven through the lead plate to hit the alumina piston. **b** In a constant strain-rate experiment, the σ_1 piston is then displaced continuously; thus, frictional drag is continuous.

Consequently, the stress experienced by the sample is less than that applied to the σ_1 piston. **c** In a constant stress experiment, the load on the alumina piston is held constant by keeping the σ_1 piston still or advancing it intermittently via a servo-motor. As a result, drag by the Pb plate is negligible and the stress transferred to the sample is essentially equal to that applied to the σ_1 piston

loading once the sample reaches the target peak stress (a detailed explanation of the stress-time-displacement records is given in the Electronic Supplement). The peak axial stress applied to the σ_1 -piston contains the original run-in component, which does not have to be subtracted (as is done in constant displacement experiments) in slow-deformation constant-load experiments. Thus, the nominal value of the recorded σ_1 is transferred entirely to the sample. It therefore is justified to use the peak stress recorded in the stress-time chart (hereafter denoted by σ_1^{peak}), rather than the stress derived from the conventional hit-point (denoted by σ_1^{hit}), as the best estimate of the maximum principal stress experienced by the sample (Fig. 3). This evaluation of the magnitude of σ_1 is applied to the new and old experiments in the following sections.

Experimental method

The principle of the deformation experiments is to cut a rod from a well-characterized, natural, inclusion-bearing quartz crystal and then subject it to high deviatoric stress within the nominal field of crystal plasticity at high confining

pressure and high temperature. After the experiments, the fluid inclusions are reanalysed to test for any stress-induced changes in morphology and orientation with respect to the host crystal and in chemical composition and density (or molar volume).

Rods of 6.5 mm diameter were cut from a euhedral, freely grown quartz crystal at either 45° to the basal plane and to the c -axis, with one of the a -axes either down-dip in the section (the so-called O^+ orientation, e.g. Baëta and Ashbee 1969; Blacic and Christie 1984; Tarantola et al. 2010) or perpendicular to the crystallographic c -axis ($\perp m$). The various lengths of the rods, between 2 and 13 mm, are indicated in Fig. 4. The crystal derives from a late Alpine cleft in granite of the Aar Massif at Planggenstock, Central Alps, Switzerland. The quartz displays sharp optical extinction in cross-polarized, transmitted light. Abundant secondary fluid inclusions are arrayed along healed fractures inclined $10\text{--}20^\circ$ from the c -axis. The inclusions are between ~ 5 and $200\ \mu\text{m}$ in length. Most show euhedral quartz shapes (so-called negative quartz forms) but some are irregular. At room temperature, all the inclusions contain a vapour bubble ($\sim 15\ \text{vol.}\%$) and an aqueous liquid containing $9.7\text{--}11\ \text{mass}\%$ NaCl_{eq} (salinity

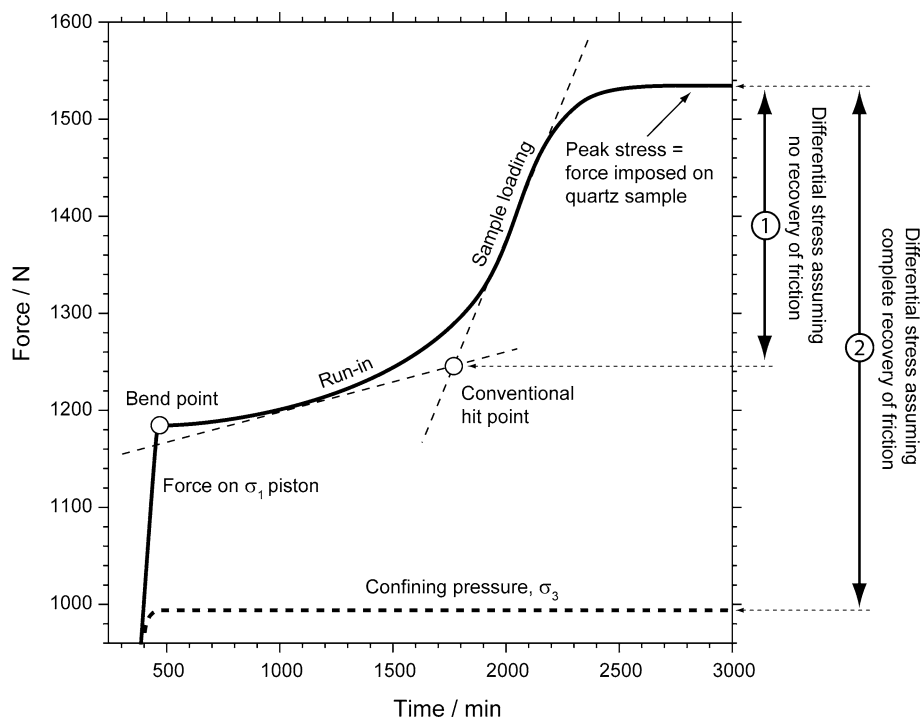
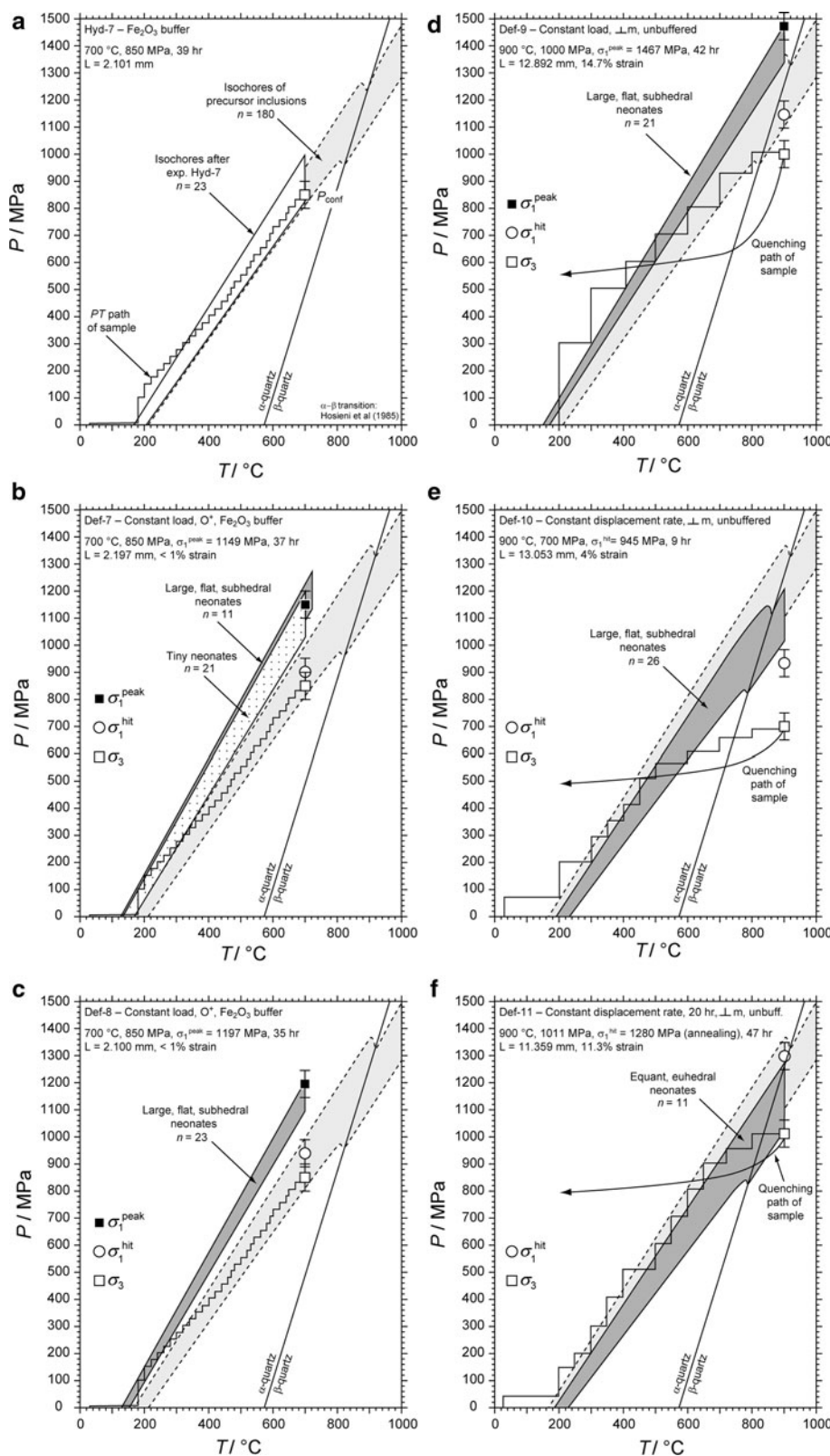


Fig. 3 Time chart of force on the σ_1 piston (thick continuous curve) and confining pressure (thick dashed curve) in the Griggs apparatus during a constant-load, deviatoric-stress experiment. The first ~ 400 min of the experiment are not shown. In normal constant displacement-rate experiments, the force absorbed by friction must be subtracted from σ_1 when calculating the differential stress. If this logic is applied to the present constant-load experiments, then the magnitude of the differential stress is given by the difference (double-

headed arrow 1) between the peak σ_1 value and the hit-point (intersection of the two tangents to the force curve above the bend-point). In the present case of constant stress experiments, friction is overcome and absorbed by the time the desired load is attained; thus, the magnitude of the differential stress is given by the difference (double-headed arrow 2) between the peak stress on the σ_1 piston and the confining pressure

Fig. 4 Results of new experiments on H₂O–NaCl inclusions in quartz. **a** Hydrostatic control experiment Hyd-7; **b–d** constant deviatoric-stress experiments Def-7,8,9; **e** constant displacement-rate deviatoric-stress experiment Def-10; **f** experiment Def-11 involving initial constant strain-rate deformation followed by annealing under constant load. *Light shading* fan of isochores of precursor inclusions; *unshaded fan* isochores of inclusions after hydrostatic experiment Hyd-7; *dark grey and stippled fans* isochores of neonate inclusions. *Open squares* magnitude of confining pressure $\sigma_3 \pm 50$ MPa at T_{exp} ; *filled squares* magnitude of peak stress $\sigma_1 \pm 50$ MPa at T_{exp} (in Def-11, this applies only to the annealing step). *Open circle* magnitude of differential stress constructed from hit-point (for comparison only). At T_{exp} , the pressures of neonate isochores show a strong shift towards σ_1^{peak} , reflecting a marked increase in their density compared to the precursors. Sample lengths are indicated by label “L”



obtained from $T_m(ice) = -6.4$ to -7.4 °C; $n = 180$; Table 1). Some inclusions contain accidentally captured crystals (i.e. not “daughter” crystals) of rutile and/or

calcite. Microthermometric, Raman microspectroscopic and laser-ablation-ICPMS analyses yield a bulk composition (in mole units) of approximately 96.1 % H₂O, 2.7 %

NaCl, 0.4 % KCl, 0.3 % CaCl₂, 0.01 % LiCl and 0.3 % CO₂. For the calculation of isochores, the minor components can be ignored, and thus, the fluid can be well approximated by the H₂O–NaCl subsystem. Homogenization occurred via a bubble-point transition at $T_h = 179\text{--}211\text{ }^\circ\text{C}$ ($n = 180$; Table 1). For each of the three samples of ~ 2 mm thickness, between 50 and 70 precursor inclusions were photographed and analysed by microthermometry and their locations were mapped photographically. The greater thickness (11.4–13 mm) of the remaining samples precluded microthermometry, but large numbers of inclusions were photographed and mapped prior to the experiments.

The P – T –salinity correlation of Bodnar and Vityk (1994) (as coded in the software package of Bakker 2003) was used to plot the internal pressure of the fluid inclusions as they are heated above T_h to the experimental temperature. The correlation takes into account both the fluid isochore and the bulk compressibility and expansivity of the quartz host. Such P – T trajectories of individual inclusions are represented by lines that emanate from the point of homogenization and that rise with almost constant slopes through the P – T plane. Each sample yields a range of T_h values, reflecting a range of inclusion densities, and therefore a range of P – T trajectories. For clarity, these have been plotted as light shaded fans in Fig. 4. Bends and kinks in these fans reflect the change in molar volume of the quartz host at and in the vicinity of the alpha–beta phase boundary (Hosieni et al. 1985). Hereafter, we refer to these P – T trajectories simply as “isochores.”

The quartz samples were sealed inside welded gold capsules (experiments Hyd-7, Def-7 and Def-8) or platinum capsules (experiments Def-9, 10, 11) and placed within the solid-medium (NaCl) Griggs apparatus. No water was added to the capsules. Figure 4 shows the stepped heating–compression paths followed to subject the samples to the experimental temperature (700 or 900 °C) and hydrostatic confining pressure (700–1,000 MPa). In the one hydrostatic experiment (Hyd-7) and in two deformation experiments (Def-7 and Def-8), the isochores of the fluid inclusions were followed as closely as possible to minimize differential pressure between the interior and exterior of the inclusions, and so avoid the possibility of irreversible (permanent) deformation. Nevertheless, the natural spread in densities of the inclusions means that some inclusions experienced up to 100 MPa of differential pressure. The hydrostatic run (Hyd-7) was performed as a control experiment to reveal any artefacts that this P – T trajectory and associated differential pressure may induce. Instead of attempting to deform the sample, it was simply cooled and decompressed along the reverse of the heating–compression path. In the other experiments (Def-7 to -11), once the desired P – T conditions were reached, the

σ_1 -piston was advanced to apply an axial compressive stress (solid σ_1 squares in Fig. 4) over periods of 9–42 h. The confining pressure thus became equivalent to the minimum principal stress (open σ_3 squares in Fig. 4), horizontally oriented and radially symmetric.

After the deformation step in experiment Def-11, the load on the σ_1 -piston was relaxed to the level of the confining pressure. The sample was then left to anneal under hydrostatic conditions at 900 °C for 47 h (Fig. 4f).

All the samples were subsequently cooled and decompressed to room conditions along the paths shown in Fig. 4. In experiments Hyd-7, Def-7 and Def-8 (Fig. 4a–c), the reverse of the heating–compression path was followed over 9 h, again to minimize the differential pressure and so avoid any irreversible deformation. In the remaining three experiments, the samples were cooled to 200 °C within 3.5 min and then cooled and decompressed to room conditions within 3 h. The P – T path of these three quenched experiments induced very high differential pressures in the inclusions. This is explicitly taken into account when discussing the results of these experiments below.

Care was taken to locate the position of the thermocouple during the experiments. For the larger samples, subsequent analyses were performed only on regions that lay within a vertical distance of ~ 2 –3 mm from the thermocouple tip, so as to avoid any effects of temperature gradients during the experiments. Additional details of the experimental method are given in Tarantola et al. (2010).

Results

The hydrothermal control experiment (Hyd-7) caused the fluid inclusions to become more euhedral and equant in shape. Their salinities in some cases have increased by up to 1.5 mass% NaCl compared to the precursors, and their T_h values show a slightly wider spread. Whereas the highest T_h values are unchanged, the lowest values are some 11 degrees lower than the precursors (Table 1). Thus, the fan of isochores calculated for the inclusions after the experiment (white field in Fig. 4a) reaches to slightly higher pressures than the fan of isochores prior to the experiment (light shaded field in Fig. 4a). This result was unexpected, because no shifts were found in the analogous hydrothermal experiments carried out by Diamond et al. (2010). In contrast to that study, individual inclusions in the present study could not be measured before and after the experiment. It is therefore impossible to tell whether the shift in $T_m(\text{ice})$ and T_h values was real and due to the P – T path of the experiment, or whether was just apparent, in that it simply reflects the full, natural range of the precursor inclusions, which was not entirely captured by the microthermometry of 180 “starting inclusions” (Table 1).

Table 1 Microthermometric data of fluid inclusions before and after high *P–T* experiments

Exp.	Basel lab no.	Type of experiment ^a	Before experiment			After (intact inclusions)			After (relict inclusions)			After (neonate inclusions)			
			<i>n</i>	<i>T_m</i> (ice) ^b (°C)	<i>T_h</i> ^c (°C)	<i>n</i>	<i>T_m</i> (ice) ^b (°C)	<i>T_h</i> ^c (°C)	<i>n</i>	<i>T_m</i> (ice) ^b (°C)	<i>T_h</i> ^c (°C)	<i>n</i>	<i>T_m</i> (ice) ^b (°C)	<i>T_h</i> ^c (°C)	
Hyd-7	164AT	Hydrostatic	69	-6.9 to -7.4 (-7.0)	179–207 (197)	23	-7.0 to -8.7 (-8.0)	168–208 (184)							
Def-7	165AT	Load	52	-6.8 to -7.2 (-7.0)	188–195 (192)	1	-10.2	175	8	-7.6 to -10.3 (-8.8)	149–178 (164)	21*	-8.0 to -10.6 (-9.1)	116–166 (146)	
Def-8	167AT	Load	59	-6.4 to -7.4 (-7.1)	194–211 (205)	3	-7.9 to -9.9 (-8.8)	186–218 (202)				23**	-9.1 to -13.0 (-10.2)	129–153 (138)	
Def-9	152ATh	Load		n.m.	n.m.							21**	-8.2 to -8.7 (-8.5)	153–176 (161)	
Def-10	186ATh	Displacement		n.m.	n.m.							26**	-7.2 to -8.5 (-7.5)	174–231 (204)	
Def-11	199ATh	Annealing		n.m.	n.m.							11**	-7.8 to -8.0 (-7.9)	186–227 (204)	

n.m., microthermometry impossible owing to thickness of samples (up to 13 mm)

^a Load: constant load, displacement: constant displacement rate

^b Melting temperature of ice upon heating. Values listed as range and mean (in brackets)

^c Homogenization temperature by disappearance of the vapour bubble. Values listed as range and mean (in brackets)

* Tiny neonate inclusions

** Large, flat, subhedral neonate inclusions

As the shift is very minor compared to that generated by the deformation experiments (presented below), its cause is immaterial. To be conservative, the spread in isochores found after experiment Hyd-7 is taken to define the precursors in all the subsequent deformation experiments (light shaded field in Fig. 4b–f).

The deformation experiments without annealing (Def-7, -8, -9 and -10) achieved plastic strains between ~ 1 and 14.7 %. The higher strains are clearly visible in the macroscopic bulging of the retrieved samples (Fig. 5a). At the microscopic scale, all the deformed samples, including the subsequently annealed sample, show undulatory optical extinction and bands of *c*-axis misorientation, both of which are diagnostic of crystal-plastic deformation in quartz. No features indicating dynamic bulk recrystallization were recognized in experiments Def-7 and Def-8. In the high-strain, constant displacement-rate experiments Def-9, -10 and -11, zones of the crystals that had been fractured during the loading process of the experiment had recrystallized to small grains. The strong microstructural modifications of the inclusions made it impossible to relocate exactly the same individual inclusions as analysed prior to the experiments. Therefore, our comparison of the

fluid inclusion properties before and after the experiments must be based only on statistical samples. This is certainly a weakness of our approach. However, as mentioned above, the results of Hyd-7 define the effective densities and salinities of the inclusions at high *P* and *T*, prior to experimental application of differential stress. This provides an adequate basis to quantify any modifications of density and salinity caused by the deformation experiments.

The initially euhedral inclusions (Fig. 5b) underwent strong shape changes in all the deformation experiments. Clusters of dismembered inclusions, consisting of flat, irregularly shaped relicts surrounded by planar haloes of tiny neonate inclusions, are common in experiments Def-7 and Def-8 (Fig. 5c). These features are identical to those reported by Tarantola et al. (2010). However, the samples are dominated by large, flat, subhedral to euhedral inclusions, lying subparallel to σ_3 (Fig. 5d). Comparison with photographs taken before the experiments shows that all these flat, euhedral inclusions are new. We therefore classify them as neonates. Similar inclusion shapes and orientations of neonate inclusions are observed in Def-9, even though significant differential pressures were generated

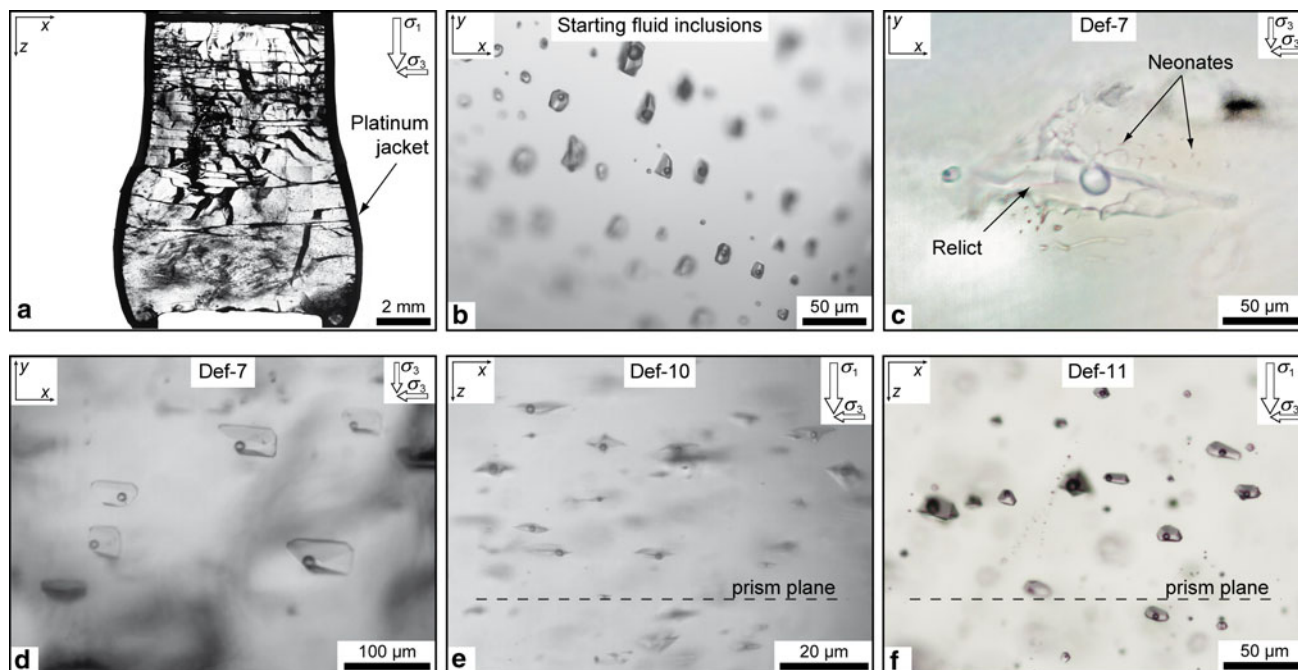


Fig. 5 Room-temperature photographs of the hydrothermal quartz crystal from Planggenstock, Aar Massif, Switzerland, used for deformation experiments. **a** Quartz rod after high-strain experiments (e.g. Def-9,10,11) showing barrelling due to crystal-plastic deformation; **b** precursor (pre-deformation) saline aqueous fluid inclusions. The inclusions are large and mostly euhedral, indicating microstructural equilibrium with the host crystal; **c** details of deformed fluid inclusion after experimentally straining the host crystal under high deviatoric stress in a Griggs piston-cylinder apparatus. View down to

σ_1 (*z*-axis) into the radially symmetric plane of σ_3 (*x*, *y* axes). The inclusion is dismembered, and its irregular shape indicates microstructural disequilibrium; **d** large, flat, subhedral neonate (newly formed) inclusions observed after experiment Def-7. View as in **c**; **e** deformed inclusions elongated along a crystallographic prism plane; **f** euhedral fluid inclusions observed after deformation and subsequent annealing. The inclusions show only a weak preferred orientation but otherwise no other features of a deformation history. View along a σ_3 -axis (*y*) into a σ_1 - σ_3 plane (*x*, *z* axes)

during the heating–cooling trajectory and during quenching and even though σ_3 and σ_1 lay on opposite sides of the alpha–beta quartz transition (which involves a $\sim 1\%$ change in volume of the host quartz). In the constant displacement-rate experiment (Def-10), the precursor inclusions had high initial overpressures ($P_{\text{incl}} \gg P_{\text{conf}}$), but the changes in shapes were quite similar to those of the other experiments. The inclusions are more flattened parallel to σ_3 , and their vertical cross-sections are more lens-shaped (Fig. 5e). After the annealing experiment (Def-11), all the inclusions remaining in the sample are neonates with equant, euhedral shapes (Fig. 5f). Their long axes are aligned subparallel to σ_3 .

The neonate inclusions in the three experiments buffered by Fe_2O_3 contain no detectable gases other than the trace CO_2 that was present in the precursors. Inclusions in the unbuffered experiments gained variable amounts of H_2 via diffusional transport into the sample jacket from the piston-cylinder assembly, as described by Diamond et al. (2010). Most of the H_2 reacted with the CO_2 in the inclusions to produce CH_4 . The molar ratios of CH_4/CO_2 in the neonate inclusions thus vary between 0 and 1, but total carbon was conserved. When present, excess H_2 makes up at most 0.33 mol% of the inclusions. These changes in gas compositions have no appreciable effect on the bulk density of the inclusions compared to their precursors.

In the experiments in which the inclusions experienced internal underpressures with respect to σ_1 (Fig. 4b–d), all the neonate inclusions are markedly denser than their precursors (Table 1). The increase in density is demonstrated by their lower homogenization temperatures ($T_{\text{h}} = 116\text{--}166\text{ }^\circ\text{C}$) and higher salinities (12–17 mass% NaCl_{eq} , based on $T_{\text{m}}(\text{ice}) = -8.0$ to $-13.0\text{ }^\circ\text{C}$) compared to the precursors ($T_{\text{h}} = 179\text{--}211\text{ }^\circ\text{C}$ and $T_{\text{m}}(\text{ice}) = -6.4$ to $-7.4\text{ }^\circ\text{C}$; see data Table in the Electronic Supplement). Thus, the isochores that emanate from the T_{h} values at the base of the diagrams rise with steeper P/T slopes (shown in Fig. 4b–d by dark shaded and stippled fans, truncated at T_{exp}). The most remarkable result is that, in each experiment, the densest of the neonate isochores (that with highest P at T_{exp}) intersects σ_1^{peak} at T_{exp} .

Experiment Def-10 was a constant displacement-rate experiment, and therefore, because σ_1 changes continuously rather than attaining a plateau, no σ_1^{peak} value is shown in Fig. 4e. The experiment was performed with $P_{\text{incl}} \gg P_{\text{conf}}$. Here too the neonate inclusions show a slight increase in salinity (10.7–12.3 mass% NaCl_{eq} , based on $T_{\text{m}}(\text{ice}) = -7.2$ to $-8.5\text{ }^\circ\text{C}$), but in contrast to the other experiments, which have $P_{\text{incl}} < P_{\text{conf}}$, the T_{h} values increased slightly (174–231 $^\circ\text{C}$). As a consequence, the lowest density isochore of the neonates (low- P boundary of the light shaded fan in Fig. 4e) lies close to σ_1^{hit} at T_{exp} .

In experiment Def-11 (Fig. 4f), the isochores of the neonate inclusions span the pressure range between σ_3 and σ_1^{hit} . Their salinities are around 1 mass% NaCl_{eq} , higher than the precursors, and the T_{h} values have increased slightly (186–227 $^\circ\text{C}$). The first stage of this experiment involved deformation at a constant displacement rate and the second involved annealing under hydrostatic conditions at $P_{\text{conf}} = \sigma_3$. By analogy with the other experiments, all of the neonate inclusions are deduced to have formed during the first stage in response to the high deviatoric stresses. Thus, some of the isochores of these inclusions pass through σ_1^{hit} , as expected. However, some isochores also pass through σ_3 . These are interpreted to be neonates that decreased their density during the second annealing stage, their final internal pressures reaching the value of σ_3 . The behaviour of the neonates during the second stage is thus in line with previous experiments under hydrostatic conditions (Sterner and Bodnar 1989; Bakker and Jansen 1991; Vityk and Bodnar 1995).

Discussion of new experimental results

The only change induced in the fluid inclusions during control experiment Hyd-7 was a ripening of their shapes towards more perfectly euhedral quartz forms. This spontaneous process, which minimizes interfacial energy between phases in contact, takes place via thermally activated dissolution and reprecipitation of quartz on the inclusion walls. The process has been widely observed in natural and synthetic inclusions (Roedder 1984; Gratier and Jenatton 1984; Bodnar 2003) and was accordingly expected in our experiments. Otherwise, the minor changes in density in experiment Hyd-7 confirms that, at least for the two experiments in which the heating–compression paths closely followed the inclusion isochores (Def-7 and Def-8), no significant artefacts were induced by our experimental method.

Most of the parameters of our 700 $^\circ\text{C}$ experiments are comparable to those in Tarantola et al. (2010) and Diamond et al. (2010), but the inclusions in the present study display markedly stronger changes in shape. Four methodological differences that may explain this result are as follows: (1) The present experiments were carried out under higher confining pressure (850 MPa versus 600 MPa); (2) They involved $\text{H}_2\text{O}\text{--}\text{NaCl}$ inclusions, whereas the earlier work used $\text{CO}_2\text{--}\text{H}_2\text{O}\text{--}\text{NaCl}$ inclusions. Entering these differences in pressure and fluid composition into the quartz solubility equation of Akinfiyev and Diamond (2009), the solubility of quartz within the fluid inclusions is approximately 1.4 times higher in the present study (0.6 molal $\text{SiO}_{2,\text{aq}}$) than in the earlier work (0.42 molal $\text{SiO}_{2,\text{aq}}$); (3) The present experiments involved much

larger precursor inclusions (100–200 μm long vs. 20–50 μm long); and (4) Fluid inclusions are far more abundant in the new samples than in those of the previous studies. From these differences, we conclude that large inclusions deform more easily, that more abundant inclusions permit more extensive quartz deformation, and that the higher confining pressure promotes ripening of the inclusion shapes towards equilibrium forms via the elevated solubility of quartz. We also attribute the lack of relict inclusions in experiments Def-8 to Def-11 to these effects, in that pronounced deformation should eventually destroy all relicts by the progressive spawning of more and more neonate inclusions.

Regarding the increase in density of the neonates, it is clear that fluid inclusions cannot simply shrink (or expand, for that matter) without generating a space problem in the adjacent quartz lattice. Nevertheless, the texturally ripened inclusions have undoubtedly acquired higher densities. Combining the results of Tarantola et al. (2010) and Diamond et al. (2010) with those of the present work, it appears that fluid inclusions must first become dismembered before their densities can change. Only the neonate inclusions adopt or approach the density commensurate with the magnitude of σ_1^{peak} . As deformation progresses, the relicts continue to spawn neonates until they are annihilated. Under conditions that promote morphological ripening (long periods at high temperature and high pressure), the clusters of neonate inclusions coalesce and form large, flat, euhedral inclusions, which are oriented perpendicular to the direction of σ_1 (Fig. 5d). Once the deviatoric stress has been removed, the inclusions adopt more equant euhedral shapes, as demonstrated by our long-term annealing experiment (Fig. 4f). Complete morphological ripening obliterates any evidence within the fluid inclusions of the previous deformation event.

The coalescence of adjacent neonate inclusions requires transfer of water and solutes through the intervening quartz. Diamond et al. (2010) showed that the formation of neonates involves loss of H_2O to the quartz host and that this process catalyses crystal-plastic deformation. In our present annealing experiment, not only the hallmarks of deformation were eradicated from the fluid inclusions, but the deformation features in the quartz host crystal were also obliterated. Thus, in our experiments, lattice recovery was accompanied by H_2O mobility. This indicates that the transfer of H_2O through the quartz may play a role in promoting recovery (Tullis and Yund 1989), in the same way as it aids deformation (e.g. Paterson 1989; Fitz Gerald et al. 1991).

Finally, it is notable that the deformed fluid inclusions are flattened subparallel to σ_3 , irrespective of the orientation of the host crystal. In experiments Def-7 and Def-8,

the quartz rod was set in the O^+ orientation, as it was in the experiments of Tarantola et al. (2010). In both the new and old experiments, flattening of the inclusions occurred within a crystallographic rhomb plane that was inclined just a few degrees away from σ_3 . In experiments Def-9 and Def-10, the quartz rod was set in the $\perp\text{m}$ orientation, and flattening occurred within a prism plane that was oriented subparallel to σ_3 . Thus, flattening occurs within the crystallographic plane that lies closest to perpendicularity with σ_1 . The flattening of each inclusion is facilitated by semi-brittle microfracturing, as described by Tarantola et al. (2010). The orientations of the microfractures at very high angles to σ_1 (rather than parallel to σ_1 as in mode-I fractures) are the result of the “hoop” stress concentration increasing normal to the largest compressive stress with increasing confining pressure (Goodier 1933; Hirth and Tullis 1989; Wanamaker et al. 1990; Tarantola et al. 2010, their Fig. 11). The strict alignment of the many thousands of flattened inclusions within each sample defines a true cleavage within the deformed quartz. Presumably, other orientations of the host crystal within the stress field would activate other crystallographic cleavage planes.

Discussion of previous experimental results

The results of the new constant-load experiments presented in Fig. 4b–d demonstrate a systematic approach of the neonate isochores to the value of σ_1^{peak} , rather than to σ_1^{hit} . This confirms our argument that the fluid inclusions experience the peak stress applied to the σ_1 -piston in the Griggs rig. This finding can now be used to adjust the analogous P – T diagrams in the previous experiments of Diamond et al. (2010). Prior to doing this, however, an improvement can also be made in the construction of the CO_2 – H_2O – NaCl isochores used to interpret the Diamond et al. (2010) results.

Diamond et al. (2010) were unable to estimate meaningful absolute internal pressures of the various types of inclusions at T_{exp} (700 °C), owing to the uncertainty in applied stresses discussed above. Their study therefore emphasized the relative differences in internal pressures between the neonate, relict and intact inclusions (via Eq. 9 in Diamond et al. 2010). Now, with the magnitudes of the applied stresses known, a better attempt can be made at estimating the absolute internal pressures of the inclusions, as follows.

The chemical compositions and bulk molar volumes (densities) of all the precursor and modified inclusions were determined by Diamond et al. (2010) from analyses near room temperature. The internal pressures of the inclusions at 700 °C can be estimated from these low-

temperature data if a means is found to extrapolate the pertinent isochores to very high pressures. For the CO_2 – H_2O – NaCl compositions in question, two equations of state (EoS) are available in the literature to perform the extrapolation. The first is the Duan et al. (1995) EoS, as corrected by Bakker (2003). The experimental data to which this EoS is fitted are limited to $P \leq 300$ MPa and $T \leq 550$ °C (Gehrig 1980), but the EoS is claimed to be valid up to 500 MPa and 700 °C. The Anderko and Pitzer (1993) EoS for H_2O – NaCl , which underlies the Duan et al. (1995) formulation, is likewise valid to 500 MPa at 700 °C. The second equation is the Bowers and Helgeson (1985) EoS, which is also fitted to the same experimental data of Gehrig (1980). Figure 6 shows examples of the very similar isochores that are predicted by the two EoS for a ternary composition and a bulk molar volume ($21 \text{ cm}^3 \text{ mol}^{-1}$) typical of the neonate inclusions analysed by Diamond et al. (2010). Also shown in Fig. 6 are the experimental data of Gehrig (1980) for 4 isochores (20.7, 21, 22 and $25 \text{ cm}^3 \text{ mol}^{-1}$) emanating from the isoplethic solvus. In detail, this data set is not perfectly isochoric, owing to artefacts of the experimental method described by Gehrig (1980), but in the present context the error can be neglected.

It can be seen in Fig. 6 that the two predicted isochores lie at significantly higher pressures than the experimental measurements, which they are supposed to fit. Extrapolation of the EoS isochores to 700 °C therefore seems certain to overestimate the true pressures. Fortunately, all four experimental isochores plotted in Fig. 6 have linear P/T slopes. This being the case, simple linear extrapolation of the Gehrig (1980) data is probably the most reliable means to estimate the fluid pressure at 700 °C. Thus, a pressure of 917 MPa is obtained for the $21 \text{ cm}^3 \text{ mol}^{-1}$ isochore illustrated in Fig. 6, whereas the EoS predictions yield values of 1,147 and 1,133 MPa for the same input data. The final step in calculating the internal pressure of the fluid inclusions at 700 °C is to correct for the expansion and compression of the alpha-quartz host crystal between the low P – T conditions at which the input compositions and molar volumes were measured, and the P – T conditions of the Griggs rig experiments. The short-dashed line in Fig. 6 shows the effect of this correction (calculated using the EoS for quartz given by Hosieni et al. 1985) on the linearly extrapolated isochore. Hence, for the example modelled inclusion in Fig. 6 with $V_m = 21 \text{ cm}^3 \text{ mol}^{-1}$, the internal pressure at 700 °C is estimated to be ~ 884 MPa.

This approach has been used in the present study to calculate the absolute internal pressures of the neonate fluid inclusions reported by Diamond et al. (2010). Figure 7 displays the resulting updated P – T diagrams for 4 deformation experiments. The fans of isochores for the neonate

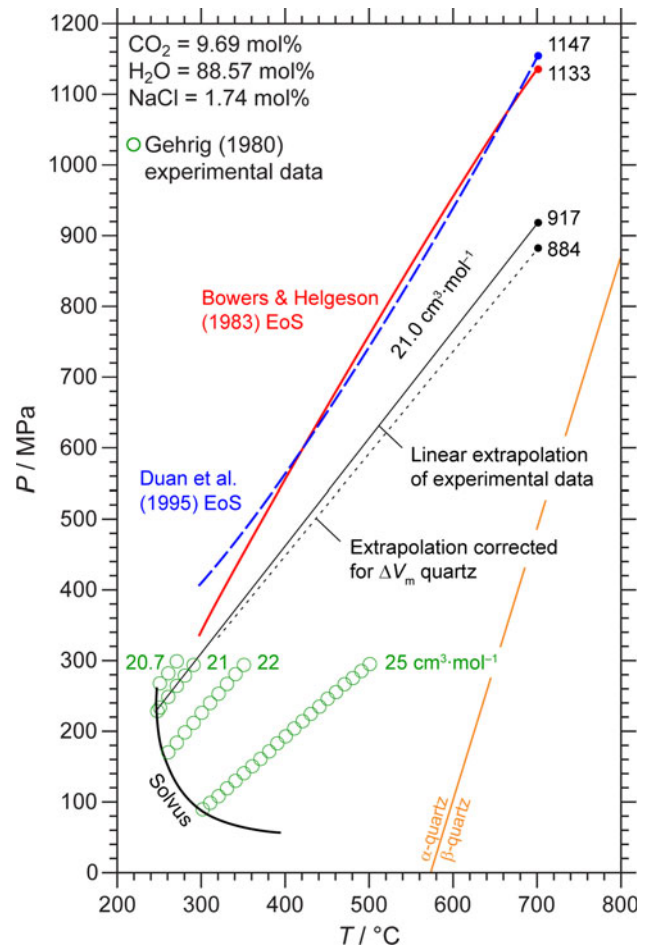
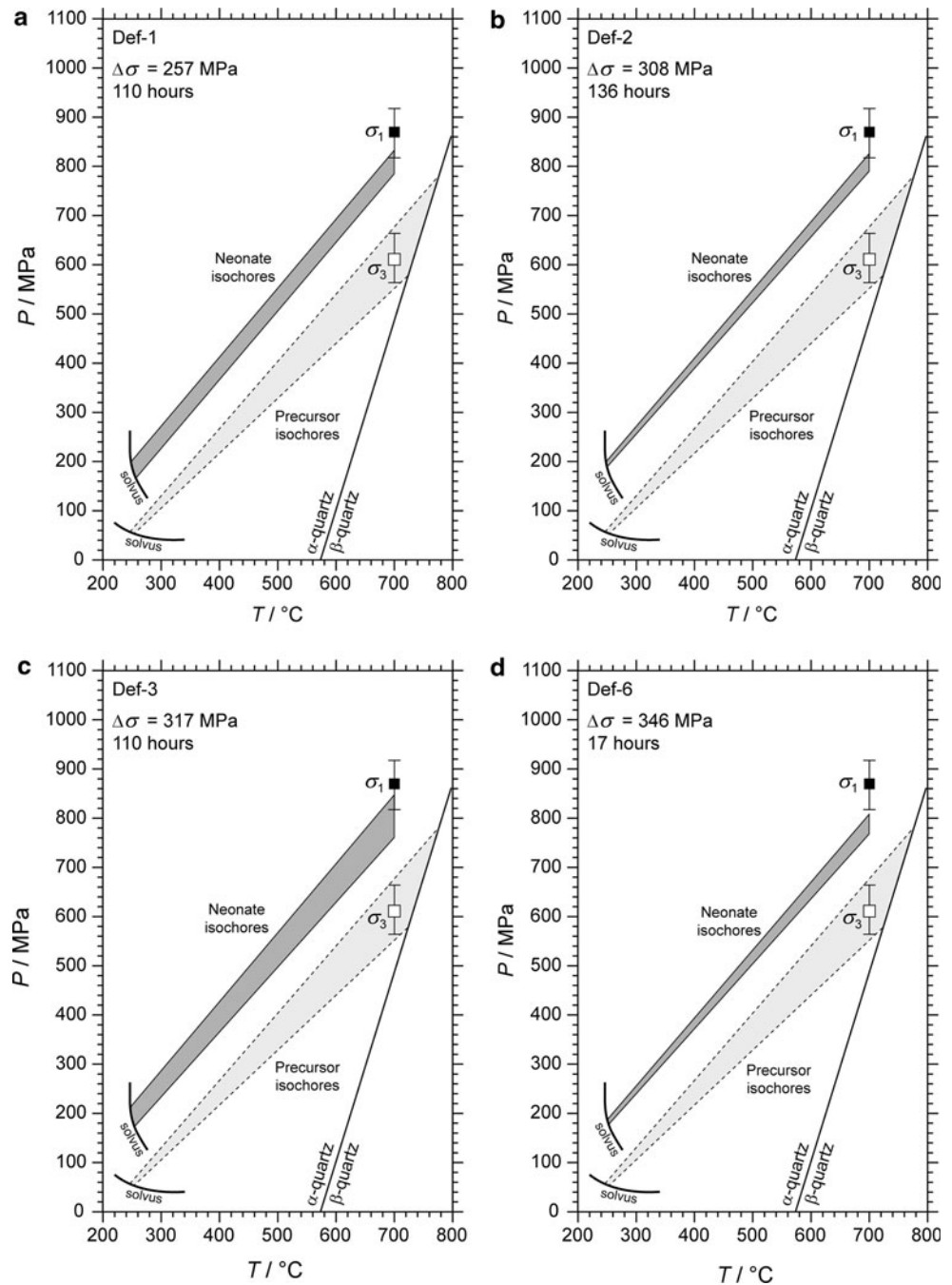


Fig. 6 Illustration of approach taken to construct isochores of modified CO_2 – H_2O – NaCl inclusions following the deformation experiments. Example isochores predicted for a molar volume of $21 \text{ cm}^3 \text{ mol}^{-1}$ using the Duan et al. (1995) and Bowers and Helgeson (1985) equations of state (blue and red curves, respectively) lie at pressures significantly above the isochoric experimental data of Gehrig (1980). A more plausible prediction of fluid pressure at 700 °C is obtained by extrapolating the experimental isochores linearly (thin continuous line), then correcting for the expansion and compression of the quartz host crystal (short-dashed line)

inclusions (Fig. 7, dark shading) show a consistent shift to higher pressures than their precursors, reflecting their increased densities. Also plotted in Fig. 7 are the peak stress values (σ_1^{peak}) of the experiments. It is clear that the isochores of the densest neonate inclusions at 700 °C tend to approach the maximum principal stress imposed during the deformation experiments. The short duration of experiment Def-6 presumably explains the small increase in density of the neonate inclusions compared to the other experiments. These results are entirely consistent with the new experiments on H_2O – NaCl inclusions presented in Fig. 4. The question raised by Diamond et al. (2010), as to why the neonate inclusions unexpectedly tend to equilibrate with σ_1 instead of with the mean stress $(\sigma_1 + 2\sigma_3)/3$, remains unanswered.

Fig. 7 Updated plots of experimental results in Diamond et al. (2010; their Fig. 10). Details of isochore construction are given in the text. Constant-load experiments showing shifts in the fans of isochores for neonate inclusions (dark grey) compared to precursor inclusions (light grey). The shift of the neonate isochores to higher pressures is due to their increase in density during the deformation experiments. The densest neonate isochores approach the maximum principal stress applied to the samples, σ_1



Conclusions

The deformation-induced changes in the H₂O–NaCl fluid inclusions in the new experiments are thoroughly consistent with the previous results of Tarantola et al. (2010) and Diamond et al. (2010), which were obtained from experiments on CO₂–H₂O–NaCl inclusions. In part the new observations represent more advanced steps along a progression in modifications of density, composition and shape, all caused by high deviatoric stresses. The plane of flattening of the intact and relict inclusions lies

subperpendicular to σ_1 , regardless of the orientation of the host crystal. Each deformed sample consequently displays one true crystallographic cleavage (on rhomb, prism or presumably other planes) defined by the alignment of the flattened inclusions.

Our reassessment of the stress corrections in constant-load Griggs-type experiments implies that the quartz samples do indeed experience the peak stress applied to the σ_1 piston, rather than a lower value obtained by the hit-point corrections of the stress-time-displacement chart in constant displacement-rate experiments. When plotted in

P – T diagrams with the isochores of modified H_2O – NaCl inclusions, it becomes clear that this peak axial stress drives the observed increase in density of the neonate inclusions.

This new insight into the effective magnitude of σ_1 during the experiments, in combination with a more accurate method to extrapolate CO_2 – H_2O – NaCl isochores to the experimental temperatures, has permitted us to calculate the absolute pressures involved in the previous experiments by Diamond et al. (2010). It is found that these earlier experiments display the same relationship between density of neonate inclusions and magnitude of σ_1 as found in the new experiments. It therefore seems beyond doubt that the density of the neonates tends towards an internal pressure commensurate with $P = \sigma_1$ at T_{shearing} , and not with $P = \sigma_{\text{mean}}$, as would seem more intuitively obvious. The rate of density change appears to be promoted by large-sized precursor inclusions, high differential stresses, long periods at high P and high T , and fluid compositions that maximize quartz solubility.

Although still untested on natural samples, these results support the proposal of Tarantola et al. (2010) that deformed fluid inclusions can serve as monitors of both the orientation and magnitude of σ_1 during low-strain, ductile deformation of quartz-bearing rocks.

Acknowledgments We thank Mrs Lagoutte and Mr and Mrs Fouchet of Montauroux for finding and returning to us the only copy of our raw data, which had been stolen from our vehicle during a fieldtrip in southern France. We appreciate the very helpful and constructive comments on the manuscript by A. Kronenberg and an anonymous journal reviewer.

References

- Akiniev NN, Diamond LW (2009) A simple predictive model of quartz solubility in water-salt- CO_2 systems at temperatures up to 1000 °C and pressures up to 1000 MPa. *Geochim Cosmochim Acta* 73:1597–1608
- Anderko A, Pitzer KS (1993) Phase equilibria and volumetric properties of the system KCl – H_2O and NaCl – KCl – H_2O above 573 K: EoS representation. *Geochim Cosmochim Acta* 57:4885–4897
- Baěta RD, Ashbee KHG (1969) Slip systems in quartz: I. Experiments. *Am Mineral* 54:1551–1574
- Bakker RJ (2003) Package FLUIDS 1. Computer programs for analysis of fluid inclusion data and for modeling bulk fluid properties. *Chem Geol* 194:3–23
- Bakker RJ, Jansen JBH (1991) Experimental post-entrapment water loss from synthetic CO_2 – H_2O inclusions in natural quartz. *Geochim Cosmochim Acta* 55:2215–2230
- Bakker RJ, Jansen JBH (1994) A mechanism for preferential H_2O leakage from fluid inclusions in quartz, based on TEM observations. *Contrib Mineral Petrol* 116:7–20
- Blacic JD, Christie JM (1984) Plasticity and hydrolytic weakening of quartz single crystals. *J Geophys Res* 89:4223–4239
- Bodnar RJ (2003) Re-equilibration of fluid inclusions. In: Samson IM, Anderson AJ, Marshall DD (eds) *Fluid inclusions: analysis and interpretation*. Min Ass Canada, short course series, vol 32, pp 213–232
- Bodnar RJ, Vityk MO (1994) Interpretation of microthermometric data for H_2O – NaCl fluid inclusions. In: De Vivo B, Frezzotti ML (eds) *Fluid inclusions in minerals, methods and applications*. Virginia Tech, Blacksburg, pp 117–130
- Bowers TS, Helgeson HC (1985) FORTRAN programs for generating fluid inclusion isochores and fugacity coefficients for the system H_2O – CO_2 – NaCl at high pressures and temperatures. *Comput Geosci* 11:203–213
- Diamond LW, Tarantola A, Stünitz H (2010) Modification of fluid inclusions in quartz by deviatoric stress. II: experimentally induced changes in inclusion volume and composition. *Contrib Mineral Petrol* 160:845–864
- Duan ZH, Møller N, Weare JH (1995) Equation of state for the NaCl – H_2O – CO_2 system: prediction of phase equilibria and volumetric properties. *Geochim Cosmochim Acta* 59(14):2869–2882
- Fitz Gerald JD, Boland JN, McLaren AC, Ord A, Hobbs BE (1991) Microstructures in water-weakened single crystals of quartz. *J Geophys Res* 96(B2):2139–2155
- Gehrig M (1980) Phasengleichgewichte und PVT-Daten ternären Mischungen aus Wasser, Kohlendioxid und Natriumchlorid bis 3 kbar und 550 °C. Doctoral Dissertation, University of Karlsruhe
- Goodier TN (1933) Concentration of stress around spherical and cylindrical inclusions and flaws. *Trans ASME APM* 55–57:39–44
- Gratier JP, Jenatton L (1984) Deformation by solution-deposition, and re-equilibration of fluid inclusions in crystals depending on temperature, internal pressure and stress. *J Struct Geol* 6(1/2):189–200
- Hall DL, Sterner SM (1995) Experimental diffusion of hydrogen into synthetic fluid inclusions in quartz. *J Metamorph Geol* 13:345–355
- Hirth G, Tullis J (1989) The effects of pressure and porosity on the micromechanics of the brittle-ductile transition in quartzite. *J Geophys Res* 94(B12):17825–17838
- Hollister LS (1990) Enrichment of CO_2 in fluid inclusions in quartz by removal of H_2O during crystal-plastic deformation. *J Struct Geol* 12(7):895–901
- Holyoke CW III, Kronenberg A (2010) Accurate differential stress measurement using the molten salt cell and solid salt assemblies in the Griggs apparatus with applications to strength, piezometers and rheology. *Tectonophysics* 494:17–31
- Hosieni KR, Howald RA, Scanlon MW (1985) Thermodynamics of the lambda transition and the equation of state of quartz. *Am Mineral* 70:782–793
- Johnson EL, Hollister LS (1995) Syndeformational fluid trapping in quartz—determining the pressure–temperature conditions of deformation from fluid inclusions and the formation of pure CO_2 fluid inclusions during grain-boundary migration. *J Metamorph Geol* 13(2):239–249
- Kerrick R (1976) Some effects of tectonic recrystallization on fluid inclusions in vein quartz. *Contrib Mineral Petrol* 59:195–202
- Kronenberg AK, Tullis J (1984) Flow strengths of quartz aggregates: grain size and pressure effects due to hydrolytic weakening. *J Geophys Res* 89:4298–4312
- Mavrogenes JA, Bodnar RJ (1994) Hydrogen movement into and out of fluid inclusions in quartz—experimental evidence and geologic implications. *Geochim Cosmochim Acta* 58:141–148
- Morgan GB, Chou IM, Pasteris JD, Olsen SN (1993) Re-equilibration of CO_2 fluid inclusions at controlled hydrogen fugacities. *J Metamorph Geol* 11:155–164
- Paterson MS (1989) The interaction of water with quartz and its influence in dislocation flow—an overview. In: Shun-ichiro K

- (ed) Rheology of solids and of the earth. Oxford University Press, Oxford, pp 107–142
- Renner J (1996) Experimentelle Untersuchung zur Rheologie von Coesit. Berichte des Instituts für Geophysik der Ruhr-Universität Bochum, Reihe A, vol 48, 178 pp
- Roedder E (1984) Fluid inclusions. Mineralogical society of America. Rev Mineral 12:646
- Schmatz J, Schenk O, Urai J (2011) The interaction of migrating grain boundaries with fluid inclusions in rock analogues: the effect of wetting angle and fluid inclusion velocity. Contrib Mineral Petrol 162:193–208
- Sternner SM, Bodnar RJ (1989) Synthetic fluid inclusions—VII. Re-equilibration of fluid inclusions in quartz during laboratory-simulated metamorphic burial and uplift. J Metamorph Geol 7:243–260
- Sternner SM, Hall DL, Keppler H (1995) Compositional re-equilibration of fluid inclusions in quartz. Contrib Mineral Petrol 119:1–15
- Tarantola A, Diamond LW, Stünitz H (2010) Modification of fluid inclusions in quartz by deviatoric stress I: experimentally induced changes in inclusion shapes and microstructures. Contrib Mineral Petrol 160:825–843
- Tullis J, Yund RA (1989) Hydrolytic weakening of quartz aggregates: the effects of water and pressure on recovery. Geophys Res Lett 16(11):1343–1346
- Vityk MO, Bodnar RJ (1995) Textural evolution of synthetic fluid inclusions in quartz during reequilibration, with applications to tectonic reconstruction. Contrib Mineral Petrol 121:309–323
- Wanamaker BJ, Wong TF, Evans B (1990) Decrepitation and crack healing of fluid inclusions in San Carlos olivine. J Geophys Res 95(B10):15623–15641
- Wilkins RWT, Barkas JP (1978) Fluid inclusions, deformation and recrystallization in granite tectonites. Contrib Mineral Petrol 65:293–299